


Article

Fatigue Reliability Based on Predicted Posterior Stress Ranges Determined from Strain Measurements of Wind Turbine Support Structures

Marko Kinne ^{1,*} and Sebastian Thöns ^{1,2} ¹ Bundesanstalt für Materialforschung und -prüfung (BAM), 12205 Berlin, Germany² Division of Structural Engineering, Lund University, 22100 Lund, Sweden

* Correspondence: marko.kinne@bam.de

Abstract: In the present paper, an approach for updating the continuous stress range distribution of a welded connection of a wind turbine support structure with predicted information from strain measurements is presented. Environmental conditions, such as wind or, in offshore fields, waves and currents, in combination with rotor excitations generate cyclic stresses affecting the reliability of welded joints of the support structure over the service life. Using strain measurements, these conditions can be monitored, and the resulting stress ranges, under consideration of measurement, mechanical and material uncertainties, can be reconstructed. These stress ranges can be used as an input for updating the prior probability density function (PDF) of the stress ranges predicted by the overall dynamics and a detailed design analysis. Applying Bayesian probability theory and decision theoretical implications, the predicted posterior probability density of the stress ranges is calculated based on the design information and uncertainties. This approach is exemplified, and it is shown how the predicted stress ranges and the design stress ranges are distributed. The prior and the predicted posterior stress ranges are used for a reliability calculation for potentially entering a pre-posterior decision analysis.

Keywords: Bayesian updating of stress ranges; posterior fatigue reliability; strain measurements of wind turbine support structures



Citation: Kinne, M.; Thöns, S. Fatigue Reliability Based on Predicted Posterior Stress Ranges Determined from Strain Measurements of Wind Turbine Support Structures. *Energies* **2023**, *16*, 2225. <https://doi.org/10.3390/en16052225>

Academic Editor: José António Correia

Received: 21 December 2022

Revised: 10 February 2023

Accepted: 16 February 2023

Published: 25 February 2023



Copyright: © 2023 by the authors. Licensee MDPI, Basel, Switzerland. This article is an open access article distributed under the terms and conditions of the Creative Commons Attribution (CC BY) license (<https://creativecommons.org/licenses/by/4.0/>).

1. Introduction

Wind turbines with fixed support structures, which are used for the conversion of wind energy to electric power with little to no greenhouse gas emissions, consist of different components, e.g., in the turbine part (the blades or the generator) and the structural part (the support structure). Over the service life, the components are exposed to different environmental loads, such as wind and, additionally in offshore fields, waves and currents, in combination with the excitation by the rotor, which can lead to damage and, if applicable, to failure of the whole wind turbine. For a safe and accident-free operation of wind turbines over the service life, condition monitoring (of the movable parts) and structural health monitoring (of the static components) can be installed. To monitor the load on the static components, e.g., the monopile, strain gauges can be applied to the outer surface to record its actual strain and determine the stress state.

In the design phase of wind turbines, various factors related to the turbine and the structural part have to be considered. The location of the wind turbines, with the characteristics of the wind field and the geographical conditions, but also the legal requirements must be considered. Subsequently, the layout of the turbine, including the movable parts, i.e., the rotor blades, the hub, the gear box and the generator, and also the nacelle has to be designed appropriately to find the optimal configuration for energy production. Based on the layout and characteristics of the turbine part and considering the climate and geographical conditions, the support structure of the wind turbine can be designed, e.g., as a

monopile, a jacket structure or a floating type. The design of the turbine and the structure are an iterative process, considering changes and adjustments. In this process, different developers and manufacturers work together due to the complexity of wind turbines [1,2].

During the design phase of wind turbines, their time dependent behavior is modelled with probabilistic engineering models considering uncertainties, e.g., in the environmental conditions, in the model itself and in the material, to calculate and forecast the reliability. By using data from the installed monitoring systems, the uncertainty in the design phase can be reduced and predictions about the further behavior can be made more accurately. However, the latter point requires the modelling of relevant uncertainties for the measurement of stress ranges. Furthermore, repair and maintenance planning requires the forecasting of stress ranges and the utilization of both the prior (designed) and the measured stress ranges, i.e., the calculation of the predicted posterior stress ranges.

In the field of structural reliability, knowledge on stress ranges is fundamental, as it is included in the reliability calculation (e.g., [3,4]). In the context of structural integrity management using decision analysis, it is often beneficial to collect additional information prior to making a decision [5]. This information can be obtained from measurements, which facilitates a posterior decision analysis. The information can also be predicted, which results in a pre-posterior decision analysis [6]. In wind turbines, several measuring systems can be installed, e.g., acceleration sensors [7] or strain gauges (as considered in this publication), which can be used to collect information about conditions of the component or structure and for updating prior data on the stress ranges.

Based on the above reasoning, an approach is presented to determine how (1) the prior data on the stress ranges from the design can be used to forecast stress ranges to be measured with an uncertain measurement system and (2) the forecasted stress ranges can be adapted by the prior stress ranges to calculate the predicted posterior stress ranges.

In the first part, based on design information about the stress resultants, the prior probability density function of the stress ranges is determined based on material and mechanical models considering uncertainties. Using predicted strain measurements, which are also derived from the prior information of the stress resultants, and considering the uncertainty in the measurement process, the materials and the mechanical models, the resulting stresses ranges are determined and used as input for updating the prior stress range distribution. Applying Bayesian probability theory, the predicted posterior stress range distribution is determined according to Bayes' theorem.

In the second part, the reliability of a welded joint is calculated considering the prior and the predicted posterior stress ranges.

2. Decision Theoretical Background

Pre-posterior decision analysis pursues the aim of optimizing decisions by collecting additional yet unknown information in combination with the information actions [8–10]. Fields of application of the pre-posterior decision analysis include, for example:

- The design of monitoring systems;
- The optimization of inspection and maintenance operations;
- The planning required for the design of experiments;
- The decisions about the detail of the model.

General pre-posterior decision analyses are composed of information management, system state management and utility, as shown in Figure 1.

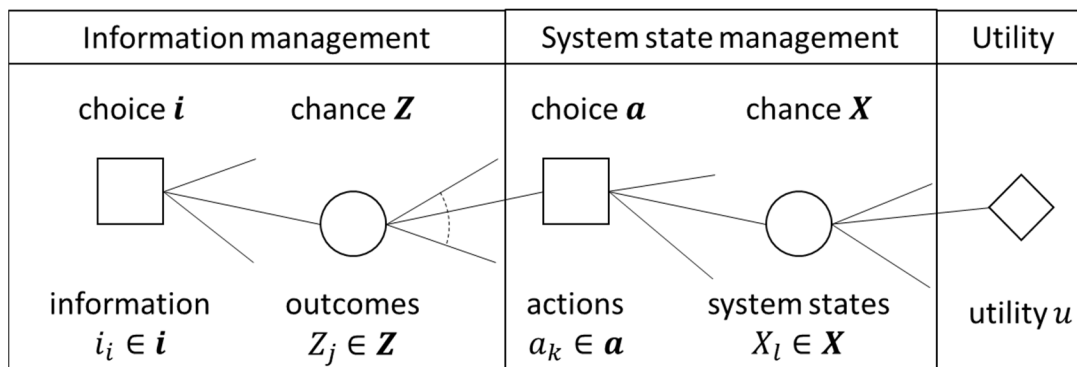


Figure 1. General overview of pre-posterior decision analysis.

Choice nodes are visualized as rectangles and chance nodes are shown as circles, while the utility node is a visualized as a diamond. The aim is to find the optimal information acquirement strategy, i_i , together with the corresponding outcome-dependent actions, a_k , to maximize the expected pre-posterior utility, U_{pp} :

$$U_{pp} = \max_{i_i \in \mathbf{i}} E_{Z_j} \left[\max_{a_k \in \mathbf{a}} E_{X_l | Z_j} [u(i_i, Z_j, a_k, X_l)] \right] \tag{1}$$

Various solutions of the objective function (Equation (1)) in normal and extensive analysis formulation have been produced in recent decades [11]. Most commonly, the information outcome, Z_j , is modelled as an event defined by a limit state function (see, e.g., [12]). The information outcome event is used for posterior updating of the system states. The system states are defined as discrete states to facilitate the allocation of the utility model, which is associated with discrete safe, failure and damage states. For the event of damage, i.e., $X_{l=1} = D$, the system state is described with the limit state function, $g(\Theta)$, and the inequality $g(\Theta) < 0$ (Θ) is denoted as the vector of uncertain input variables.

Measurement outcomes are in many cases continuously distributed, especially related to continuous measurements. The outcome $Z_j = Z$ is then distributed with the probability density function $f_Z(z)$. One or more of the limit state function random variables Θ can then be updated depending on the physical relation to the measurand. The joint, i.e., pre-posterior, probability density function for parameters of the system state, $f_{\Theta, Z}(\theta, z)$, is defined by the conditional probability definition for continuous distributions:

$$f_{\Theta, Z}(\theta, z) = f_{\Theta | Z}(\theta | z) \cdot f_Z(z) = f_{Z | \Theta}(z | \theta) \cdot f_{\Theta}(\theta) \tag{2}$$

It should be noted that for the decision theoretical extensive formulation, i.e., the calculation and sampling of the posterior distribution $f_{\Theta | Z}(\theta | z) = \frac{1}{c} \cdot f_{Z | \Theta}(z | \theta) \cdot f_{\Theta}(\theta)$ with $c = \int_{\Theta} f_{Z | \Theta}(z | \theta) \cdot f_{\Theta}(\theta) d\theta$, non-direct solutions have been developed by Markov Chain Monte Carlo approaches [13–15].

The conditional probability distribution of the outcome given the system states $f_{Z | \Theta}(z | \theta)$ may be defined as the likelihood given the (already obtained) observations. The likelihood approach facilitates that the uncertainties caused by, e.g., the deviations in the mechanical and measurement processes, are captured and modelled. Limitations in the view of the authors are that that in the context of a pre-posterior decision analysis, the observations are not given but predicted based on the prior model and that an explicit model of measurement uncertainty is lacking. The latter point may prevent measurement system development and innovation, as the relevant measurement system performance characteristics may not be identified (see, e.g., [16,17]).

For the specific situation that fatigue relevant stress ranges are determined with strain gauge measurements and rainflow counting (e.g., [18]), the random variable stress ranges based on measured strains, $\Delta\sigma_M$, are the outcome Z . The design calculation of the stress

ranges is represented by the random variable $\Delta\sigma_{Design}$. The predicted posterior probability density function (Equation (2)) can then be rewritten as:

$$f(\Delta\sigma_{Design}|\Delta\sigma_M) = \frac{1}{c} \cdot f(\Delta\sigma_M|\Delta\sigma_{Design}) \cdot f(\Delta\sigma_{Design}) \quad (3)$$

with $c = \int_{\Delta\sigma_{Design}} f(\Delta\sigma_M|\Delta\sigma_{Design}) \cdot f(\Delta\sigma_{Design}) d\Delta\sigma_{Design}$.

Application of Strain Measurements in Structural Health Monitoring

In structural health monitoring, for the determination of stress resultants, which are caused by external loads affecting the structure, the measurement of elongations often provides the initial position. Besides optical measurement methods, such as fiber optic sensors or digital image correlation with high-resolution cameras, electrical measurement methods, usually in the form of strain gauges, are commonly used [19,20]. The advantages of strain gauges are that they are low cost, easy to install and precise [21]. The use of strain measurements in structural health monitoring over a period of time and its evaluation can be found in various research fields, e.g., in the prognosis of aircraft engine components based on a fracture mechanics model [22]. Strain measurements are input into the reliability calculation to update fatigue reliability and for further predictions of the component or system [23]. One of the first examples of the application of strain measurements to assess the fatigue of wind turbines was described in [24]. By using monitoring data, a more precise calculation of the fatigue life compared to that determined at the design phase could be made, as shown in [25], where the fatigue life of the principal structural components of the tower were significantly higher.

3. Framework for the Calculation of the Predicted Posterior Stress Ranges in Wind Turbine Support Structures

The first part of Section 3 details the determination of the continuous predicted posterior stress range PDF based on predicted stress ranges using strain measurements. The uncertainty in the strain measurement process is described in Section 3.2, while in Section 3.3, the calculation of the stress resultants from the determined strains is described in detail. In Section 3.4, the correlation model between the uncertainty parameters is explained.

3.1. Determination of Predicted Posterior Stress Ranges Based on Predicted Strains

For the determination of the predicted posterior probability of the stress ranges, $f(\Delta\sigma_{Design}|\Delta\sigma_M)$, the prior distribution of the stress ranges, $f(\Delta\sigma_{Design})$, is updated with predicted stress ranges, $f(\Delta\sigma_M|\Delta\sigma_{Design})$, based on strain which results from the prior knowledge of the system:

$$f(\Delta\sigma_{Design}|\Delta\sigma_M) = \frac{1}{c} \cdot f(\Delta\sigma_M|\Delta\sigma_{Design}) \cdot f(\Delta\sigma_{Design}) \quad (4)$$

The approach for the determination of predicted posterior stress ranges is shown in Figure 2.

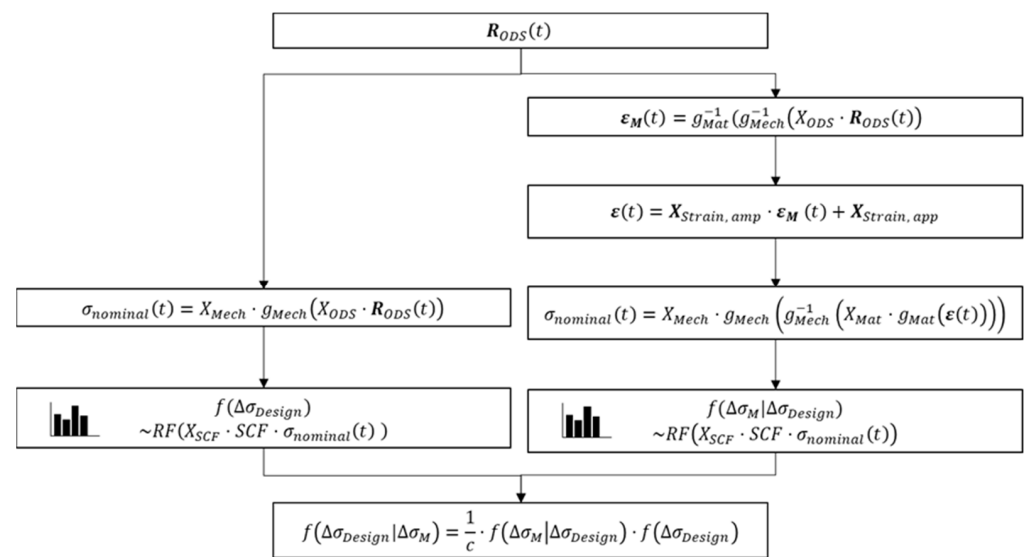


Figure 2. Scheme for the determination of the predicted posterior stress ranges, $f(\Delta\sigma_{Design}|\Delta\sigma_M)$. The models are described by $g()$, while the uncertainties are abbreviated with X . RF describes the rainflow counting algorithm.

On the left side of Figure 2, the determination of the prior stress ranges is shown, while on the right side the determination of the predicted stress ranges based on strain is visualized.

A detailed explanation of the determination of the prior stress ranges and the stress ranges based on the predicted strain measurements is described below.

For the determination of the stress ranges based on predicted strain measurements, $f(\Delta\sigma_M|\Delta\sigma_{Design})$, the starting point is the data of stress results from the design, $R_{ODS}(t)$.

The uncertainty in the simulation of the stress results from the design process is modelled with the overall dynamic simulation uncertainty, X_{ODS} , which is multiplied by the stress results. The uncertainty includes [26,27]:

X_{dyn}	Uncertainty related to the modelling of the dynamic response, including the uncertainty in damping ratios and eigenfrequencies;
X_{st}	Uncertainty connected with the assessment of the wind climate;
X_{exp}	Uncertainty related to the modelling of the exposure (site assessment), such as the terrain roughness and the landscape topography.

The overall dynamic simulation uncertainty is then calculated as:

$$X_{ODS} = X_{dyn} \cdot X_{st} \cdot X_{exp} \tag{5}$$

When an offshore wind turbine is considered, the uncertainty in the wave loading, X_{wave} , has to be included in the overall dynamic simulation uncertainty.

Based on the stress results, the measured strains, $\epsilon_M(t)$, at the measurement positions (red dots in Figure 4) are calculated by:

$$\epsilon_M(t) = g_{Mat}^{-1} \left(g_{Mech}^{-1} (X_{ODS} \cdot R_{ODS}(t)) \right) \tag{6}$$

The inverse material model, $g_{Mat}^{-1}()$, describes the calculation from the corresponding stresses $\sigma(t)$, $\tau(t)$ to the measured strains, assuming linear elastic material behavior and a plane stress state. The inverse mechanical model, $g_{Mech}^{-1}()$, describes the relation of the determination of the stresses $\sigma(t)$, $\tau(t)$ from the corresponding forces and moments, in

this case $X_{ODS} \cdot R_{ODS}(t)$. A detailed explanation of the material and mechanical model can be found in Section 3.3.

Due to uncertainty in the strain measurement process, the measured strains are subject to measurement uncertainties, for example:

$$\varepsilon(t) = X_{Strain, amp} \cdot \varepsilon_M(t) + X_{Strain, app} \quad (7)$$

The amplifier strain measurement uncertainty, $X_{Strain, amp}$, contains the uncertain amplifying deviation factor, the model uncertainty associated with the gauge factor correction model, the gauge factor variation and the temperature coefficient of the gauge factor. The apparent strain measurement uncertainty, $X_{Strain, app}$, includes the model uncertainty, the uncertain amplifier zero deviation and the model uncertainty of the temperature variation curve. A detailed model of the measurement uncertainties can be found in Section 3.2.

Using the strains, $\varepsilon(t)$, the nominal stress, $\sigma_{nominal}(t)$, can be determined by using the material and mechanical model including the related uncertainties X_{mat} and X_{Mech} (e.g., at the welded joint) by:

$$\sigma_{nominal}(t) = X_{Mech} \cdot g_{Mech} \left(g_{Mech}^{-1} (X_{Mat} \cdot g_{Mat}(\varepsilon(t))) \right) \quad (8)$$

The individual calculation steps in Equation (8) are described in the following by Equations (9)–(11).

The normal and the shear stresses, $\sigma(t)$, $\tau(t)$, at the position of the strain gauges using the material model $g_{Mat}()$ are determined based on the calculated strains, $\varepsilon(t)$:

$$[\sigma(t), \tau(t)] = X_{Mat} \cdot g_{Mat}(\varepsilon(t)) \quad (9)$$

The uncertainty in the material model, X_{Mat} , is modelled by the Young's modulus, E , and the Poisson ratio, ν , as random variables. Variations in the Young's modulus and the Poisson ratio along the circumference are normally small and can be neglected [28].

The determined stresses are used for the calculation of the stress resultants, $R(t)$. The relation between the normal and shear stresses and the stress resultants is given by an inverse use of the mechanical model, $g_{Mech}^{-1}()$. The stress resultants are in the same section as the strain measurement:

$$R(t) = g_{Mech}^{-1}(\sigma(t), \tau(t)) \quad (10)$$

The stress resultants are input for the calculation of the nominal stress, $\sigma_{nominal}(t)$, in the same section by using the mechanical model, $g_{Mech}()$:

$$\sigma_{nominal}(t) = X_{Mech} \cdot g_{Mech}(R(t)) \quad (11)$$

The nominal stress considers macro-geometric effects and describes the stress in a structural component [29]. The uncertainty in the mechanical model itself is in accordance with the probabilistic model code of the Joint Committee of Structural Safety (JCSS), modelled with the random variable X_{Mech} [28]. The random variable is multiplied by the model output. Although the mechanical model is used twice in the determination of the nominal stress, the model uncertainty is only considered once, as the model does not change.

Based on the nominal stresses, the hot spot stresses, $\sigma_{hot\ spot}(t)$, are calculated with the stress concentration factor, SCF , and by considering the uncertainty in the stress concentration factor with X_{SCF} [27]:

$$\sigma_{hot\ spot}(t) = X_{SCF} \cdot SCF \cdot \sigma_{nominal}(t) \quad (12)$$

SCF accounts for the local stress concentrations due to the geometric discontinuities in the welded joint without consideration of the weld geometry [30] (Figure 3).

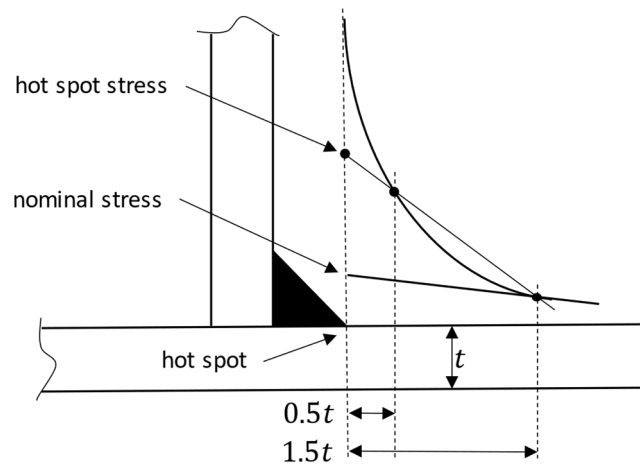


Figure 3. Different stress levels applied in SN fatigue analyses, adopted from [29].

The stress ranges, $f(\Delta\sigma_M|\Delta\sigma_{Design})$, result from the hot spot stress, $\sigma_{hot\ spot}(t)$, using the rainflow counting algorithm, $RF()$ [18]. The algorithm counts the stress ranges and cycles in the stress history:

$$f(\Delta\sigma_M|\Delta\sigma_{Design}) \sim RF(\sigma_{hot\ spot}(t)) = RF(X_{SCF} \cdot SCF \cdot \sigma_{nominal}(t)) \quad (13)$$

The prior distribution of the stress ranges, $f(\Delta\sigma_{Design})$, is directly determined based on the stress resultants from the design, $\mathbf{R}_{ODS}(t)$. Using the probabilistic mechanical model, $X_{mech} \cdot g_{Mech}()$, based on the stress resultants and the overall dynamic simulation uncertainty, X_{ODS} , the nominal stress, $\sigma_{nominal}(t)$, is calculated by:

$$\sigma_{nominal}(t) = X_{Mech} \cdot g_{Mech}(X_{ODS} \cdot \mathbf{R}_{ODS}(t)) \quad (14)$$

As introduced above, the prior stress ranges, $f(\Delta\sigma_{Design})$, are determined using the rainflow counting algorithm which counts stress ranges and cycles in the stress history of the hot spot stress (Equations (12) and (13)).

3.2. Uncertainty Modelling in the Strain Measurement Process

The strain ε , which can be determined by a strain gauge (cf. Equation (7)), can be described as the sum of the amplifier strain, ε_{amp} , the apparent strain, ε_{app} and the model uncertainty, B_p [31]:

$$\varepsilon = B_p + \varepsilon_{amp} + \varepsilon_{app} \quad (15)$$

The amplifier strain denotes the strain which is measured with the strain gauges and the amplifier, while the apparent strain results from temperature effects in the strain gauge.

The strain measurement is an electrical process, where small changes in the voltage in a circuit are measured. Commonly, the Wheatstone bridge concept in a quarter bridge configuration with one active strain gauge is used. Based on this arrangement, the measured strain, ε_M , is the ratio between the amplifier supplies voltage, U_B , and the corresponding bridge output voltage, U_A , considering the batch specific gauge factor k [32]:

$$\varepsilon_M = \frac{4 U_A}{k U_B} \quad (16)$$

Due to the influence of various uncertain factors, the measured strain, ε_M , is not identical with the mechanical strain, ε . Their general relation is given by Equation (15) and shown in more detail in the following process equation [33]:

$$\varepsilon = B_p + \frac{f_{aa}}{c_k(\mathbf{X}_k, T)} \varepsilon_M + f_{az} + \varepsilon_T(\mathbf{X}_T, T) \quad (17)$$

where B_p describes the model uncertainty, f_{aa} is the uncertain amplifying deviation factor, is the uncertain amplifier zero deviation and T is the temperature of the substrate, which is also measured.

The uncertainty of the gauge factor and its correction is described by $c_k(\mathbf{X}_k, T)$:

$$c_k(\mathbf{X}_k, T) = 1 + B_s + f_{s,v} + f_{s,q} + \alpha_k \cdot (T - T_{ref}) \tag{18}$$

where B_s represents the model uncertainty associated with the gauge factor correction model, $f_{s,v}$ is the gauge factor variation and $\alpha_k \cdot (T - 20^\circ\text{C})$ models the temperature variation of the gauge factor. $f_{s,q}$ is the transverse strain correction factor, described by the transverse sensitivity, q (Equation (19)), the Poisson ratio, ν_0 , and ε_q and ε_l , which represent the actual strains perpendicular and parallel to the primary axis of the strain gauge, respectively:

$$f_{s,q} = \frac{q}{1 - q\nu_0} \left(\frac{\varepsilon_q}{\varepsilon_l} + \nu_0 \right) \tag{19}$$

To compensate computationally for the temperature drift of the sensor, $\varepsilon_T(\mathbf{X}_T, T)$ is introduced. This quantity is referred to as the apparent strain and is defined as:

$$\varepsilon_T(\mathbf{X}_T, T) = \hat{\varepsilon}_T(T) + B_T \cdot (T - T_{ref}) \tag{20}$$

where $B_T \cdot (T - 20^\circ\text{C})$ is the model uncertainty of the temperature variation curve and $\hat{\varepsilon}_T(T)$ is a batch specific temperature variation curve [34]:

$$\hat{\varepsilon}_T(T) = -31.8 + 2.77 T - 6.55 \cdot 10^{-2} T^2 + 3.28 \cdot 10^{-4} T^3 - 3.26 \cdot 10^{-7} T^4 \tag{21}$$

3.3. Reconstruction of Stress Resultants from Strain Measurements at Tubular Sections

Using the information of elongation from the strain gauges, which are applied to the outer surface of the wind turbine support structure, the stress resultants (axial force N_x , shear forces V_y and V_z , bending moments M_y and M_z and torsional moment M_x) in this cross-section can be determined (Equations (9) and (10)) [31]. The measuring positions of the strain rosettes, $i = 1, 2, 3$, shown as red dots, are evenly distributed around the circumference (Figure 4a).

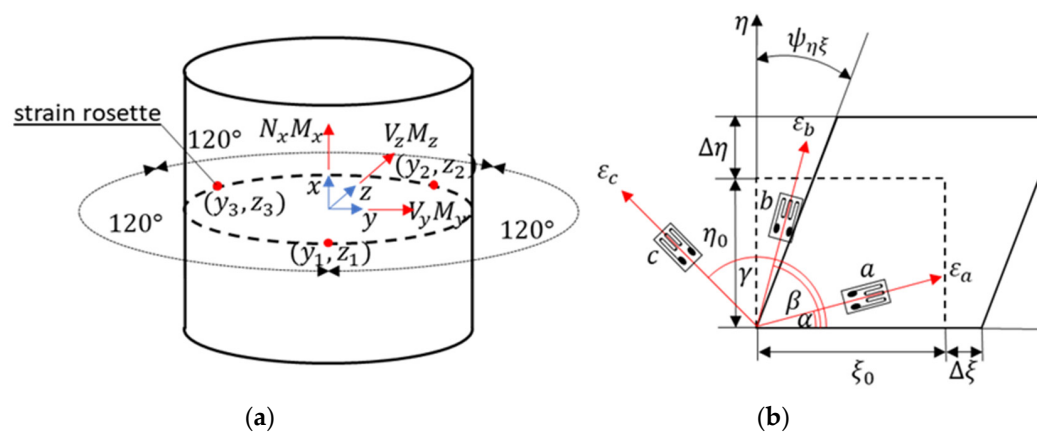


Figure 4. (a) Cross-section along a tubular steel wind turbine tower with three strain rosettes positioned around the section’s circumference marked as red dots and (b) illustration of the strain rosette applied on the surface of the steel tube consisting of three strain gauges marked as a , b and c .

Each strain rosette consists of three strain gauges a , b and c , with a local coordinate system with coordinates (ζ_i, η_i) , where the ζ_i -axis is pointing in the tangential direction of the outer surface of the tube and the η_i -axis is aligned with the global x -axis (Figure 4b).

The top view of the cross-section, together with the measuring positions as red dots, are shown in Figure 5.

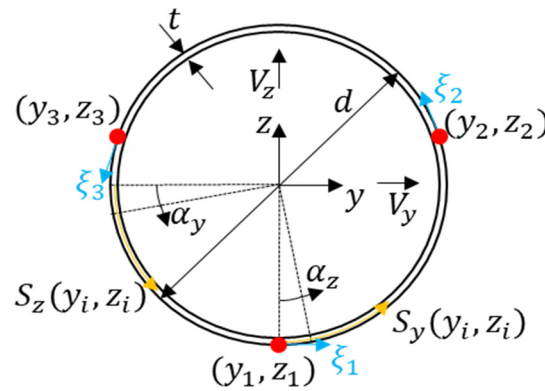


Figure 5. Top view of the cross-section marking the positions of the three strain rosettes as red dots together with the global coordinate system with coordinates (x, y, z) and local the coordinate systems with coordinates (ξ_i, η_i) , $i = 1, 2, 3$. The local η_i -axis points in the same direction as the global x -axis.

At the measuring positions, the normal strains, $\epsilon_{\eta,i}$ and $\epsilon_{\xi,i}$, and the shear strain, $\psi_{\eta\xi,i}$, of an infinitesimal material element can be determined from the mechanical strains $\epsilon_{a,i}$, $\epsilon_{b,i}$ and $\epsilon_{c,i}$ taking the angles α , β and γ into account:

$$\begin{bmatrix} \epsilon_{\xi,i} \\ \epsilon_{\eta,i} \\ \psi_{\xi\eta,i} \end{bmatrix} = \begin{bmatrix} \cos^2(\alpha) & \sin^2(\alpha) & 0.5 \cdot \sin(2\alpha) \\ \cos^2(\beta) & \sin^2(\beta) & 0.5 \cdot \sin(2\beta) \\ \cos^2(\gamma) & \sin^2(\gamma) & 0.5 \cdot \sin(2\gamma) \end{bmatrix}^{-1} \cdot \begin{bmatrix} \epsilon_{a,i} \\ \epsilon_{b,i} \\ \epsilon_{c,i} \end{bmatrix} \quad (22)$$

Assuming classical beam theory, linear elastic material behavior and a plane stress state, the normal stresses $\sigma_{\xi,i}$ and $\sigma_{\eta,i}$ and the shear stress, τ_i , can be calculated based on the previously determined strains for every measuring point:

$$\begin{bmatrix} \sigma_{\xi,i} \\ \sigma_{\eta,i} \\ \tau_i \end{bmatrix} = \frac{E}{1-\nu^2} \begin{bmatrix} 1 & \nu & 0 \\ \nu & 1 & 0 \\ 0 & 0 & 0.5 \cdot (1-\nu) \end{bmatrix} \cdot \begin{bmatrix} \epsilon_{\xi,i} \\ \epsilon_{\eta,i} \\ 2\psi_{\xi\eta,i} \end{bmatrix} \quad (23)$$

The uncertainty in the material model is modelled by the Young’s modulus, E , and the Poisson ratio, ν , as random variables [28].

Noting that $\sigma_x(y_i, z_i) = \sigma_{\eta,i}$, the relation between the section forces and moments, N_x , M_y and M_z , and the normal stress, $\sigma_x(y_i, z_i)$, at a position is given by:

$$\sigma_x(y_i, z_i) = \sigma_{\eta,i} = \frac{N_x}{A} + \frac{M_y}{I_y} z_i - \frac{M_z}{I_z} y_i \quad (24)$$

where I_y and I_z are the corresponding moment of inertia about y - and z -axis, respectively, and A is the cross-sectional area of the thin-walled tubular cross-section. Since the normal stress, $\sigma_x(y_i, z_i) = \sigma_{\eta,i}$, can be determined at each position $i = 1, 2, 3$ from the measured strains $\epsilon_{a,i}$, $\epsilon_{b,i}$ and $\epsilon_{c,i}$, it is possible to formulate a system of linear equations with unknown N_x , M_y and M_z and to solve this system of linear equations:

$$\begin{bmatrix} 1/A & z_1/I_y & -y_1/I_z \\ 1/A & z_2/I_y & -y_2/I_z \\ 1/A & z_3/I_y & -y_3/I_z \end{bmatrix} \cdot \begin{bmatrix} N_x \\ M_y \\ M_z \end{bmatrix} = \begin{bmatrix} \sigma_{\eta,1} \\ \sigma_{\eta,2} \\ \sigma_{\eta,3} \end{bmatrix} = \begin{bmatrix} \sigma_x(y_1, z_1) \\ \sigma_x(y_2, z_2) \\ \sigma_x(y_3, z_3) \end{bmatrix} \quad (25)$$

The shear stress, $\tau(y_i, z_i)$, at every measurement position can be expressed by the shear forces and torsional moment, V_y , V_z and M_x , as:

$$\tau(y_i, z_i) = \frac{M_x}{2A_m t} - \frac{V_y S_z(y_i, z_i)}{I_z t} - \frac{V_z S_y(y_i, z_i)}{I_y t} \quad (26)$$

where t is the wall thickness and $S_y(y_i, z_i)$ and $S_z(y_i, z_i)$ are the first moments of area at position i in the y - and z -direction, respectively, while I_y and I_z represent the second moments of area. Bredt's formula is used to describe the relation between the shear stress, $\tau(y_i, z_i)$, and the moment, M_x . For determining the shear forces and the torsional moment, it is possible to formulate a system of linear equations, which relates the shear stresses, $\tau(y_i, z_i)$, to the stress resultants. This system of linear equations can be solved for V_y , V_z and M_x .

$$\begin{bmatrix} 1/(2A_m t) & -S_z(y_1, z_1)/(I_z t) & -S_y(y_1, z_1)/(I_y t) \\ 1/(2A_m t) & -S_z(y_2, z_2)/(I_z t) & -S_y(y_2, z_2)/(I_y t) \\ 1/(2A_m t) & -S_z(y_3, z_3)/(I_z t) & -S_y(y_3, z_3)/(I_y t) \end{bmatrix} \cdot \begin{bmatrix} M_x \\ V_y \\ V_z \end{bmatrix} = \begin{bmatrix} \tau(y_1, z_1) \\ \tau(y_2, z_2) \\ \tau(y_3, z_3) \end{bmatrix} \quad (27)$$

Equations (23), (25) and (27) represent a material model, $g_{Mat}()$, and a mechanical model, $g_{Mech}()$, which relates the strain state to the stress resultants $\mathbf{R} = [N_x, V_y, V_z, M_x, M_y, M_z]^T$, this calculation is defined as:

$$\mathbf{R} = g_{Mech}^{-1}(g_{Mat}(\boldsymbol{\varepsilon}_1, \boldsymbol{\varepsilon}_2, \boldsymbol{\varepsilon}_3, \nu, E)) \quad (28)$$

where $\boldsymbol{\varepsilon}_i = [\varepsilon_{a,i}, \varepsilon_{b,i}, \varepsilon_{c,i}]^T$ is the vector of mechanical strain determined from strain measured by strain gauges a , b and c at position $i = 1, 2, 3$.

3.4. Correlation Model between the Uncertain Parameters

For the correlation between the parameters of process equation (Equation (17)), which describes the relation between the measured strain and the mechanical strain using strain gauges, the following assumptions are made:

- The strain gauges of the strain rosettes, which are evenly distributed around the circumference, are of the same type.
- If applicable, the strain gauges are from the same batch and thus have the same fabrication quality and production standards.
- The strain gauges are installed according to the manufacturer's instructions.
- The application of the strain gauges is in accordance with the manufacturer's instructions.
- The strain gauges are exposed to the same environmental conditions, e.g., wind speed and temperature. The spatial orientation of the strain gauges around the circumference (north, east, south and west) is neglected and thus the influence of the sun is neglected too.
- Every strain gauge is connected to its own amplifier [32,35].

The correlation between the individual uncertain strain gauge parameters, with exception to the model uncertainty, B_p , and the model uncertainty associated with the gauge factor correction model, B_s , of the process equation (Equation (17)), is assumed to be high, i.e., $\rho = 0.9$, because strain gauges of the same type are used. The correlation between the parameters of the model uncertainties, B_p and B_s , is zero, i.e., $\rho = 0$. The correlation between the uncertain amplifying deviation factor, f_{aa} , and uncertain amplifier zero deviation, f_{az} , is assumed to be zero, i.e., $\rho = 0$, as no further information on possible correlation is available. Moreover, the parameters of the gauge factor correction, $c_k(\mathbf{X}_k, T)$, are uncorrelated as no further information on the correlation is available either.

The parameters describing the material behavior, the Young's modulus, E , and the Poisson ratio, ν , are not correlated with each other, i.e., $\rho = 0$. The correlation between the Young's modulus at the different measurement positions may be neglected, i.e., $\rho = 1$.

Additionally, the correlation between the Poisson ratio at the different measuring positions is neglected, i.e., $\rho = 1$ [28].

The model uncertainties X_{dyn} , X_{st} , X_{exp} and if necessary X_{wave} , representing the overall dynamic simulation model uncertainty X_{ODS} , are not correlated with each other, i.e., $\rho = 0$, since they constitute different models.

4. Reliability of Welded Connection Determined by an SN Approach

Based on the prior and predicted posterior stress range distributions, $f(\Delta\sigma_{Design})$ and $f(\Delta\sigma_{Design}|\Delta\sigma_M)$, the fatigue reliability of the welded joint over the service life can be determined by an SN approach. This approach is based on experimental data, which are obtained by laboratory experiments and provide a functional relationship between the failure life, N , in this case the number of stress cycles to failure, and the constant stress range, $\Delta\sigma$. The general relation of a linear SN curve is given by:

$$N = K \cdot \Delta\sigma^{-m} \quad (29)$$

where K and m are constants, which are determined by the regression of the fatigue data in the logarithmic scale. Using the natural logarithm $\ln()$, Equation (29) can be rewritten as:

$$\ln(N) = \ln(K) - m \cdot \ln(\Delta\sigma) \quad (30)$$

A distinction is normally made between linear and bi-linear SN curves. For structures which are subjected to random loading and located in a corrosive environment, bi-linear SN curves are the most relevant [36]. A bi-linear SN curve is defined by:

$$N = \begin{cases} K_1 \cdot \Delta\sigma^{-m_1} & \text{for } \Delta\sigma > \Delta\sigma' \\ K_2 \cdot \Delta\sigma^{-m_2} & \text{for } \Delta\sigma \leq \Delta\sigma' \end{cases} \quad (31)$$

where $(N', \Delta\sigma')$ is the intersection of these two equations, with $N' = K_1 \cdot (\Delta\sigma')^{-m_1} = K_2 \cdot (\Delta\sigma')^{-m_2}$.

Fatigue is commonly subjected to different stress ranges and in combination with the SN curves, the Palmgren–Miner rule (hypothesis of linear damage accumulation) can be established to estimate the fatigue behavior subjected to variable amplitude loading. The hypothesis is that the damage accumulation is independent of the sequence of the applied stress cycles [37].

The fatigue damage, D_{tot} , is stated for a number of constant amplitude stress blocks and given by:

$$D_{tot} = \sum_{i=1}^q \frac{n(\Delta\sigma_i)}{N(\Delta\sigma_i)} \quad (32)$$

where q is the number of stress blocks applied, $n(\Delta\sigma_i)$ is the number of constant stress amplitude cycles for the block i with stress range $\Delta\sigma_i$ and $N(\Delta\sigma_i)$ is the number to failure for the stress range $\Delta\sigma_i$.

If the total damage accumulation, D_{tot} , which is the fraction between the stress cycles and those required for failure, exceeds a limit Δ , fatigue failure occurs (e.g., $\Delta = 1$ [37]). The limit state can be written as:

$$\Delta - D_{tot} \leq 0 \quad (33)$$

The stress cycles can be determined by using cycle counting algorithms (e.g., the rainflow counting algorithm), i.e., for every stress cycle n_i , the corresponding stress range $\Delta\sigma_i$ is calculated. In fatigue analysis, the long-term distribution of the stress ranges (in the following denoted by $f(\Delta\sigma)$) can be modelled as a continuous probability density function.

The total accumulated fatigue damage at the end of year t can be approximated by its expected value as [37]:

$$D_{tot}(t) = E \left[\sum_{i=1}^{N(t)} \Delta D_i \right] \approx E[N(t)] \cdot E[\Delta D_i] \quad (34)$$

where $E[N(t)]$ is the expected number of stress cycles and $E[\Delta D_i]$ is the expected damage increment in the time period $[0, t]$. The damage increment, $E[\Delta D_i]$, for a bi linear SN curve can be calculated as [38,39]:

$$E[\Delta D_i] = \frac{1}{K_2} \int_0^{\Delta\sigma'} (\Delta\sigma)^{m_2} f(\Delta\sigma) d\Delta\sigma + \frac{1}{K_1} \int_{\Delta\sigma'}^{\infty} (\Delta\sigma)^{m_1} f(\Delta\sigma) d\Delta\sigma \quad (35)$$

The expected number of stress cycles, $E[N(t)]$, is given by:

$$E[N(t)] = \nu \cdot t \quad (36)$$

Probabilistic and Correlation Model for the Fatigue Reliability Calculation

The application of the Palmgren–Miner rule for the calculation of the reliability of the welded connection is subjected to different uncertainties, which are related to [40]:

- Fatigue modelling (uncertainty of the validity of the SN model);
- Fatigue resistance (uncertainty of the applied SN curve);
- Fatigue loading (natural variability and uncertainty in the environmental modelling and stress calculations).

To account for the uncertainty in the Palmgren–Miner rule, the fatigue limit, Δ , is modelled as a random variable (lognormal distributed) with a mean of one [30]. The random properties of Δ can explain the deviations in real loads and conditions from those in fatigue tests and especially include the effect of variable amplitude loading [40]. The uncertainty in the SN curve on the constant amplitude fatigue resistance is modelling the parameters K_1 and K_2 as random variables (commonly normal distributed $\log(K_1)$ and $\log(K_2)$). The uncertainty in the fatigue stress estimation is composed of different factors [41]. The uncertainty in load calculation, X_{ODS} , the uncertainty in nominal stress calculation, X_{Mat} and X_{Mech} , and the uncertainty in hot-spot stress calculation, X_{SCF} , have already been considered in the determination of the stress ranges (Section 3.1). The uncertainty in the quality of detail, B_Q , is directly considered in the calculation of the expected damage increment (Equation (35)), which can be rewritten as:

$$E[\Delta D_i] = \frac{1}{K_2} \int_0^{\Delta\sigma'} (B_Q \Delta\sigma)^{m_2} f(\Delta\sigma) d\Delta\sigma + \frac{1}{K_1} \int_{\Delta\sigma'}^{\infty} (B_Q \Delta\sigma)^{m_1} f(\Delta\sigma) d\Delta\sigma \quad (37)$$

The limit state function, which describes the event of failure is given by:

$$g(\mathbf{x}_{SN}, t) = \Delta - \nu \cdot t \cdot E[\Delta D_i] \quad (38)$$

where the uncertainties associated with the SN fatigue assessment are summarized in $\mathbf{X}_{SN} = [\Delta, K_1, K_2, B_Q]^T$. The event of failure occurs if $D(\mathbf{X}_{SN}, t) = \{g(\mathbf{X}_{SN}, t) \leq 0\}$.

The uncertainties in the SN curve's intercepts K_1 and K_2 are fully correlated with each other, while the correlation between the SN curve's intercepts and the limit state Δ is zero [42]. While the random variables K_1 , K_2 and Δ are referred to in the Palmgren–Miner rule, the uncertainty in the quality of detail, B_Q , is referred to in the stress range estimation, so that the correlation between these variables is zero.

The cumulative probability of failure, $P_f(t)$, at the end of service year t is defined by integrating the joint PDF of the fatigue model parameters X_{SN} , $f(x_{SN})$ over the domain $\Omega = \{X_{SN} : g(x_{SN}, t) \leq 0\}$:

$$P_f(t) = \int_{g(x_{SN}, t) \leq 0} f(x_{SN}) dx_{SN} \quad (39)$$

which can be calculated by using the Monte Carlo simulation technique, where the annual probability of failure at service year t is given by:

$$\Delta p_f(t) = P_f(t) - P_f(t - 1) \quad (40)$$

and the corresponding annual reliability index, $\beta(t)$, is obtained from:

$$\beta(t) = -\Phi^{-1}[\Delta p_f(t)] \quad (41)$$

where $\Phi[\cdot]$ is the standardized normal distribution function.

5. Numerical Study

In the following, the approach in Section 3 for the determination of the predicted posterior stress range PDF based on predicted strain measurements in wind turbine support structures is presented in a numerical study at a monopile in Section 5.1. In Section 5.2, the predicted posteriors stress ranges are input in the fatigue calculation to recalculate the reliability and update the prior reliability according to Section 4.

5.1. Calculation of the Predicted Posterior Stress Ranges

In the design phase of wind turbines, the time-dependent behavior is simulated with a time series of the stress resultants $R_{ODS}(t)$. For the determination of the stress resultants, probabilistic engineering models are used, which consider and forecast the environmental conditions. In general, wind turbines are affected by the occurrence of wind and additionally, those offshore are effected by waves and currents [27].

For the determination of the prior stress range distribution, $f(\Delta\sigma_{Design})$, and the stress range distribution, $f(\Delta\sigma_M | \Delta\sigma_{Design})$, for updating the prior stress ranges, the stress resultants, $R_{ODS}(t)$, are derived from a simplified generic wind turbine model with a monopile support structure considering the wind speed, v_{Wind} , and the wind direction. The data on the wind direction and speed are taken from the Copernicus Marine Data Store [43]. The wind direction is divided in eight directions, from north (N), north east (NE), . . . , to west north (WN). The probability of occurrence, p , classified by the wind direction is shown in Figure 6b.

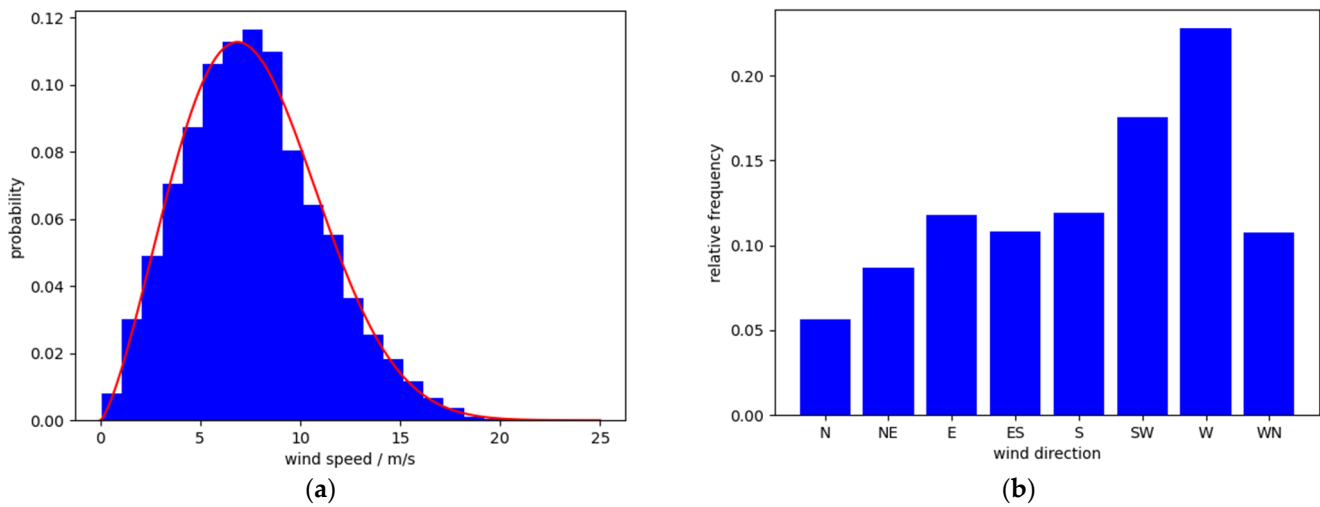


Figure 6. (a) Histogram (blue columns) of the wind speed for the wind direction east, together with fitted probability density function of the Weibull distribution (red curve). (b) Distribution of the wind direction subdivided in eight directions, from north (N), north east (NE), . . . , to west north (WN) [43].

The distribution of the wind speed is described by a Weibull distribution [44]. Based on the determined wind directions, for each wind direction, the shape and scale parameters are determined (shown in Figure 6a for the east wind direction). Thus, for each wind direction, the wind speed parameters are calculated (Table 1).

Table 1. Parameter of the wind speed depending on the wind direction.

Wind Direction	Probability of Occurrence, p	Wind Speed	
		Shape Parameter	Scale Parameter/ m/s
North (N)	0.056	1.94	7.75
North east (NE)	0.086	2.15	8.94
East (E)	0.117	2.39	8.61
East south (ES)	0.108	2.34	8.19
South (S)	0.119	2.31	8.35
South west (SW)	0.175	2.40	9.75
West (W)	0.227	2.46	9.72
West north (WN)	0.107	2.10	8.48

From the distribution of the wind speed depending on the wind direction, the moment, M_{wind} , and the force, V_{wind} , can be derived, which appear in the cross-section of the strain gauges due to the wind. Starting from the wind speed and using the Betz's Elementary Momentum Theory [1], the wind force, F_{wind} , can be determined. This force arises from the wind speed impacting the rotor blades and can be calculated as [45]:

$$F_{wind} = \frac{1}{2} c_T \rho_{air} A v_{wind}^2 \quad (42)$$

where ρ_{air} is the air density, $A = \pi \cdot \left(\frac{d_{Rotor}}{2}\right)^2$ is the area through which the air passes at velocity v_{wind} and c_T is the thrust coefficient, which is a function of the wind speed. For the calculation, a simplification is made, i.e., the thrust coefficient is assumed to be constant at $c_T = 0.6$. The wind speed at the rotor hub for the determination of the force, F_{wind} , result from the European Standard EN 61400-1 and can be calculated as [46]:

$$v_{wind}(x_{Rotor}) = v(x_{wind}) \cdot \left(\frac{x_{Rotor}}{x_{wind}}\right)^\alpha \quad (43)$$

where $v(x_{wind})$ is the measured wind speed at the maximum x_{wind} and $v_{wind}(x_{Rotor})$ is the wind speed at the maximum x_{Rotor} . α , the wind shear or power law exponent, is 0.2. Due to the large surface area, A , covered by the rotor blades and the resulting force, F_{wind} , the wind force on the pile, with a significantly lower surface area, is neglected in this simplified generic model.

The measurement of the wind speed and direction takes place at a maximum of $x_{wind} = 10$ m above ground level, while the strain gauges are installed at $x_{strain} = 20$ m above the ground level. The height of the rotor hub is $x_{Rotor} = 100$ m above the ground level (Figure 7a).

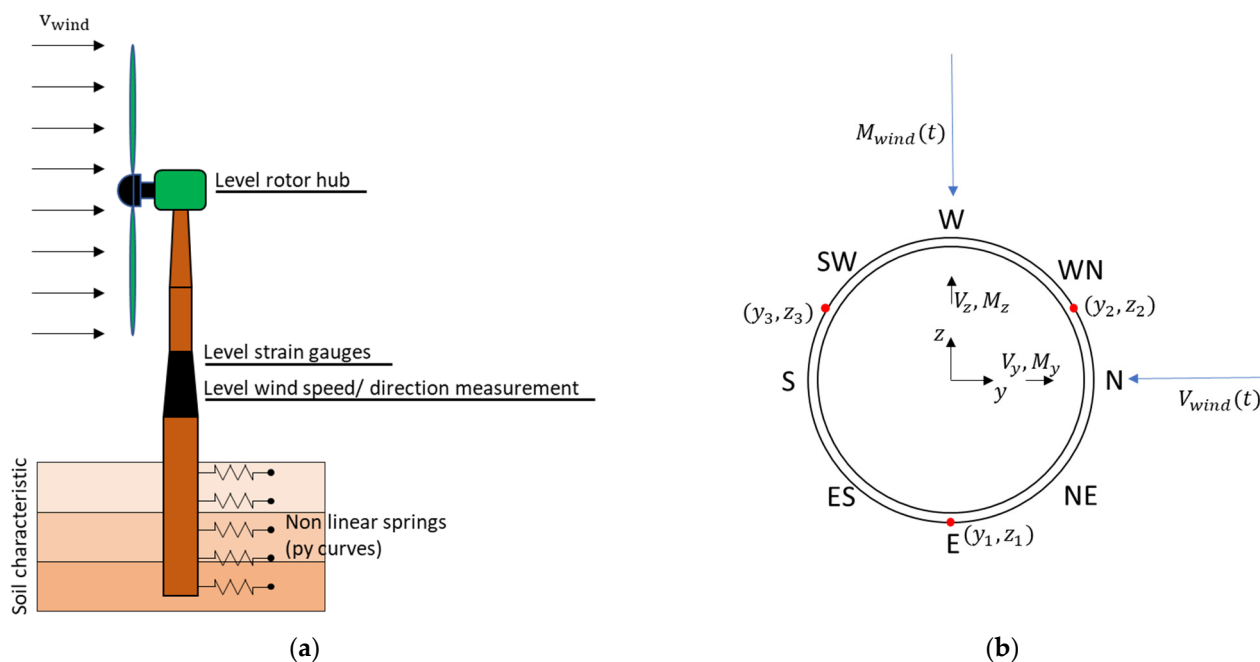


Figure 7. (a) Schematic representation of the wind turbine, (b) wind directions relative to the global coordinate system, with marked shear force, V_{wind} , and moment, M_{wind} , when the wind direction is northerly in the cross-section of the strain gauges.

For the calculation of the moment, M_{wind} , and the shear force, V_{wind} , in the cross-section of the strain gauges, a FE model with soil–pile interaction is used to consider the characteristics of the soil. The length of the pile below the sea bottom is $x_{Soil} = 50$ m [47]. The soil consists of sand at the top of small layer, followed by till, and the last layer is formed of chalk [47].

The lateral soil–structure interaction is modelled discretely with a set of independent nonlinear soil springs, which are distributed over the length of the embedded pile. The variable stiffness of the single springs is generally defined by the so-called p–y curves, which are material- and depth-dependent and describe the nonlinear soil response (i.e., the integrated subgrade reaction p) as a function of the lateral pile displacement, y , at a given depth. The p–y curves were here calculated using the IGtHPile software from the Leibnitz University [48]. In this case, and due to the lack of specific calculation methods for the till and chalk materials in the IGtHPile software, the stiff clay formulation according to Reese and Cox [49] is adopted for the main solid ground layers (till and chalk).

The structure itself is modelled as a beam, while the steel properties are modelled as linear elastic. At the top of this FE model, the calculated wind force, F_{wind} , is applied to the structure (Figure 7b). Ansys APDL software was employed for the calculation.

Based on the distribution of the wind speed given for each wind direction, the following shape and scale parameters for the bending moment and the shear force in the

cross-section of the strain gauges are determined (Table 2). The distribution can also be modelled as a Weibull distribution, similar to the distribution of the wind speed.

Table 2. Characteristic values (shape and scale parameter) of shear force, V_{wind} , and the moment, M_{wind} , using an FE model and considering the soil–pile interaction.

Wind Direction		Moment, M_{wind}		Shear Force, V_{wind}	
		Shape	Scale/Nm	Shape	Scale/N
North	(N)	0.993	7.7618×10^7	0.993	970235
North east	(NE)	1.098	1.0087×10^8	1.098	1.260×10^6
East	(E)	1.218	9.2433×10^7	1.218	1.155×10^6
East south	(ES)	1.179	8.4531×10^7	1.179	1.056×10^6
South	(S)	1.169	8.8526×10^7	1.169	1.106×10^6
South west	(SW)	1.212	1.2050×10^8	1.212	1.506×10^6
West	(W)	1.243	1.1818×10^8	1.243	1.477×10^6
West north	(WN)	1.058	9.0789×10^7	1.058	1.134×10^6

The force, $V_{wind}(t)$, and the moment, $M_{wind}(t)$, are modelled as stationary stochastic processes, i.e., the probability density function is constant over time. The underlying correlation function of the process is assumed to be of the exponential type with correlation length z [50]:

$$\begin{aligned} K_{M_{wind}M_{wind}}(\Delta t) &= Cor[M_{wind}(t), M_{wind}(t + \Delta t)] = \exp\left(-\frac{\Delta t}{z}\right) \\ K_{V_{wind}V_{wind}}(\Delta t) &= Cor[V_{wind}(t), V_{wind}(t + \Delta t)] = \exp\left(-\frac{\Delta t}{z}\right) \end{aligned} \quad (44)$$

Moreover, the force and the moment are also correlated with each other, due to the fact that both result from the same wind speed. The correlation between these values at the same point of time, $\Delta t = 0$, is assumed to be high ($\rho = 0.9$) and also exponential. Thus, the following correlation function is used:

$$K_{M_{wind}V_{wind}}(\Delta t) = Cor[M_{wind}(t), V_{wind}(t + \Delta t)] = 0.9 \cdot \exp\left(-\frac{\Delta t}{z}\right) \quad (45)$$

According to the European Standard EN 61400-1 [46], the length of the stochastic process is $t = 600$ s. The sampling rate is chosen to be 1 Hz; thus, the total number of sampling points for one stochastic process is 600.

Based on the force, $V_{wind}(t)$, the moment, $M_{wind}(t)$, and the wind direction, the stress resultants, $R_{ODS}(t)$, can be calculated using the trigonometric functions $\sin()$ and $\cos()$.

The prior stress ranges, $f(\Delta\sigma_{Design})$, from the stress resultants are determined for eight positions in the same cross-section as the strain gauges are installed. The positions are evenly distributed over the circumference (Figure 8).

Based on realizations of the stochastic process for the force, $V_{wind}(t)$, and the moment, $M_{wind}(t)$, the stress resultants can be determined and thus the nominal stress, $\sigma_{nominal}(t)$, taking the overall dynamic simulation uncertainties and the uncertainty in the mechanical model into account. For the determination of the hot spot stress, $\sigma_{hot\ spot}(t)$, from the nominal stress, the stress concentration factor SCF is multiplied, while X_{SCF} is the uncertainty in the stress concentration factor. The stress concentration factor for tubular butt weld connections is calculated according to [30]:

$$SCF = 1 + \frac{6(\delta_t + \delta_m - \delta_0)}{t} \frac{1}{1 + \left(\frac{T}{t}\right)^\beta} e^{-\alpha} \quad (46)$$

where α and β are calculated by:

$$\alpha = \frac{1.82L}{\sqrt{Dt}} \frac{1}{1 + \left(\frac{T}{t}\right)^\beta} \tag{47}$$

$$\beta = 1.5 - \frac{1.0}{\log\left(\frac{D}{t}\right)} + \frac{3.0}{\left(\log\left(\frac{D}{t}\right)\right)^2} \tag{48}$$

with D describing the outer tubular diameter, L is the length of the weld at the surface and t and T are the thicknesses of the two pipe segments, where it is assumed that there is no change in the thickness and $\delta_0 = 0.05 \cdot t$ and $\delta_t = 0.5(T - t)$.

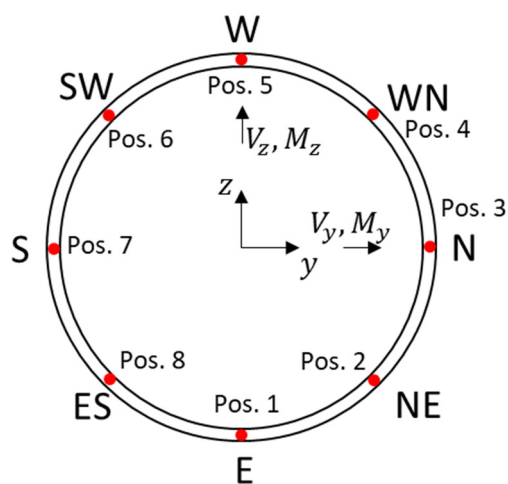


Figure 8. Positions distributed over the circumference for the determination of the stress ranges.

Thus, the hot spot stress determined from Equation (12) is input into the rainflow counting algorithm for the determination of the stress ranges (Equation (13)). Table 3 summarizes the probabilistic model parameters together with the deterministic parameters applied in the calculation of the predicted posterior stress ranges of the numerical study.

For the determination of the prior stress ranges, $f(\Delta\sigma_{Design})$, at the eight positions, for every wind direction 500 independent realizations of the stochastic process of the force, $V_{wind}(t)$, and the moment, $M_{wind}(t)$, are simulated. In fatigue analysis, the distribution of the stress ranges is described by a Weibull distribution with shape, $k_{\Delta S}$, and scale, $\lambda_{\Delta S}$, parameters [30]. The determined parameters are given in Table A1 (see Appendix A).

Based on the prior data on the stress resultants from the design, the stress ranges based on strain measurements, $f(\Delta\sigma_M | \Delta\sigma_{Design})$, are determined and forecasted as described detailed in Section 3. The uncertainties in the strain measurement process, $X_{Strain, amp}$ and $X_{Strain, app}$, and in the material, X_{Mat} , and mechanical, X_{Mech} , models, as well as the uncertainty in the stress concentration factor X_{SCF} , have to be considered.

For the determination of $f(\Delta\sigma_M | \Delta\sigma_{Design})$ at the eight positions (Figure 8) for each wind direction, 200 independent realizations of the stochastic processes of the force, $V_{wind}(t)$, and the moment, $M_{wind}(t)$, are simulated.

Table 3. Probabilistic and deterministic parameters for the calculation for the predicted posterior stress ranges.

Parameter		Unit	Distribution	Values		Reference
Model uncertainty	B_p	$\mu\text{m}/\text{m}$	normal	$\mu = 0$	$\sigma = 1$	[33]
Uncertain amplifying deviation factor	f_{aa}	-	uniform	$\mu = 1$	$\sigma = 1.73 \times 10^{-4}$	[34,51]
Uncertain amplifier zero deviation	f_{az}	$\mu\text{m}/\text{m}$	uniform	$\mu = 0$	$\sigma = 6.93 \times 10^{-1}$	[34,51]
Model uncertainty associated with the gauge factor correction model	B_s	-	normal	$\mu = 0$	$\sigma = 4.38 \times 10^{-4}$	[33]
Gauge factor variation	$f_{s,v}$	-	normal	$\mu = 0$	$\sigma = 7 \times 10^{-3}$	[34,51]
	α_k	$1/^\circ\text{C}$	normal	$\mu = 0$	$\sigma = 6.99 \times 10^{-2}$	[34,51]
Model uncertainty of the temperature variation curve	B_T	$\mu\text{m}/(\text{m K})$	normal	$\mu = 0$	$\sigma = 1.19$	[34,51]
Temperature	T	$^\circ\text{C}$	deterministic		20	[33]
Transverse sensitivity	q	-	deterministic		5×10^{-4}	[32]
Poisson's ratio	ν_0	-	deterministic		0.285	[32]
	$\varepsilon_q/\varepsilon_l$	-	deterministic		0.3	
Outer diameter	d	m	deterministic		7	
Thickness	t	m	deterministic		0.07	
Level wind direction/speed measurement	x_{wind}	m	deterministic		10	
Level strain measurement	x_{strain}	m	deterministic		20	
Level rotor hub	x_{Rotor}	m	deterministic		100	
Angle of the strain gauge	α	$^\circ$	deterministic		45	
	β	$^\circ$	deterministic		90	
	γ	$^\circ$	deterministic		135	
Young's modulus	E	N/mm^2	lognormal	$\mu = 2.1 \times 10^5$	$\sigma = 0.03 \times \mu$	[28]
Poisson's ratio	ν	-	lognormal	$\mu = 0.3$	$\sigma = 0.03 \times \mu$	[28]
Uncertainty in the mechanical model	X_{Mech}	-	lognormal	$\mu = 1$	$\sigma = 0.03$	[28]
	X_{dyn}	-	lognormal	$\mu = 1$	$\sigma = 0.125$	[26]
Uncertainties in the overall dynamic simulation	X_{wave}	-	lognormal	$\mu = 1$	$\sigma = 0.1$	[26]
	X_{st}	-	lognormal	$\mu = 1$	$\sigma = 0.03$	[26]
	X_{exp}	-	lognormal	$\mu = 1$	$\sigma = 0.15$	[26]
Uncertainty in the stress concentration factor	X_{SCF}	-	lognormal	$\mu = 1$	$\sigma = 0.05$	[27]
Length of the weld	L	m	deterministic		0.05	
Eccentricity (misalignment)	δ_m	-	deterministic		0.01	

The probability density function of the stress ranges, $f(\Delta\sigma_M|\Delta\sigma_{Design})$, is estimated by using kernel density estimation (KDE) [52], which is defined by:

$$\hat{f}_n(\Delta\sigma) = \frac{1}{nh} \sum_{i=1}^n K\left(\frac{\Delta\sigma - \Delta\sigma_i}{h}\right) \quad (49)$$

where K is representing the kernel, n is the number of determined stress ranges $\Delta\sigma_i$ and $h > 0$ is a smoothing parameter called the bandwidth. For the determination, the bandwidth is chosen as $h = 0.1$ and as a kernel, an exponential kernel is used:

$$K(\Delta\sigma, h) \propto \exp\left(\frac{\Delta\sigma}{h}\right) \quad (50)$$

Thus, as an example for the northerly wind direction at position 2, the following distribution of the stress ranges, $f(\Delta\sigma_M|\Delta\sigma_{Design})$, is given (Figure 9).

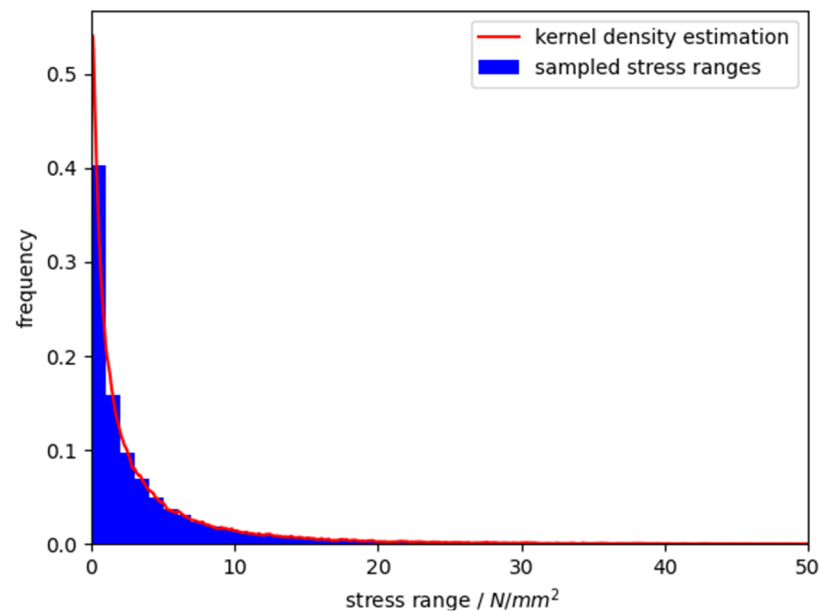


Figure 9. Histogram of the stress ranges based on strain measurements and the kernel density estimation, $f(\Delta\sigma_M | \Delta\sigma_{Design})$, at position 2 for a northerly wind direction.

With the information from the prior stress ranges and stress ranges based on strain measurements, the continuous predicted posterior stress range probability density function can be calculated according to Equation (4). The result of the probability density function at the same position 2 for a northerly wind direction is shown in Figure 10.

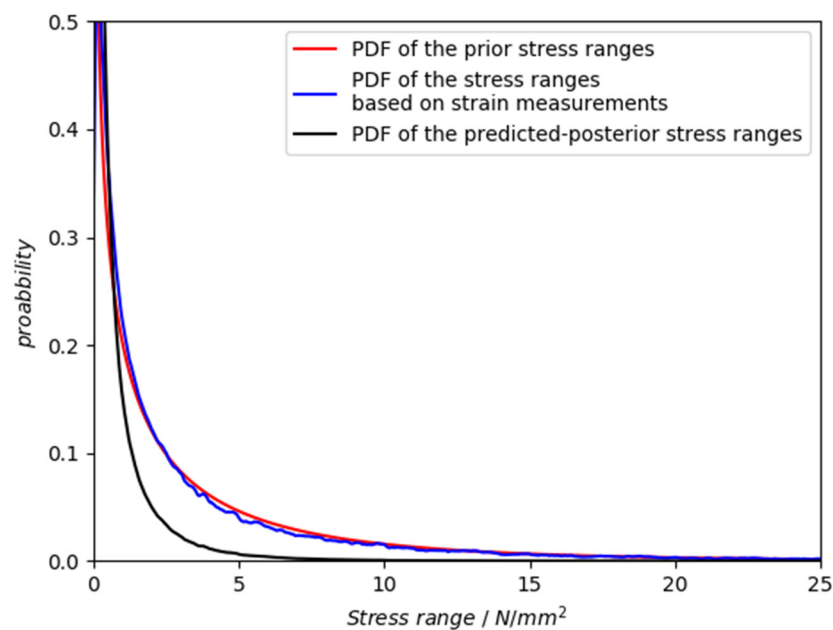


Figure 10. Graphical representation of the probability density function of the predicted posterior stress range, $f(\Delta\sigma_{Design} | \Delta\sigma_M)$, (black curve), together with the PDFs of the prior stress range, $f(\Delta\sigma_{Design})$, and the stress ranges based on strain measurements, $f(\Delta\sigma_M | \Delta\sigma_{Design})$, at position 2 for a northerly wind direction.

The difference between the probability density functions, prior and those based on strain measurements, is very small. For the determination of the influence of the uncertainties, a sensitivity analysis was performed for the design (prior) and measurements based on

the hot spot stress, $\sigma_{hot\ spot}$. The first order sensitivity indexes were calculated using a Monte Carlo Simulation (MCS) for a constant strain state with varying the uncertainties [53].

The results of the sensitivity analysis are shown in the Figure 11.

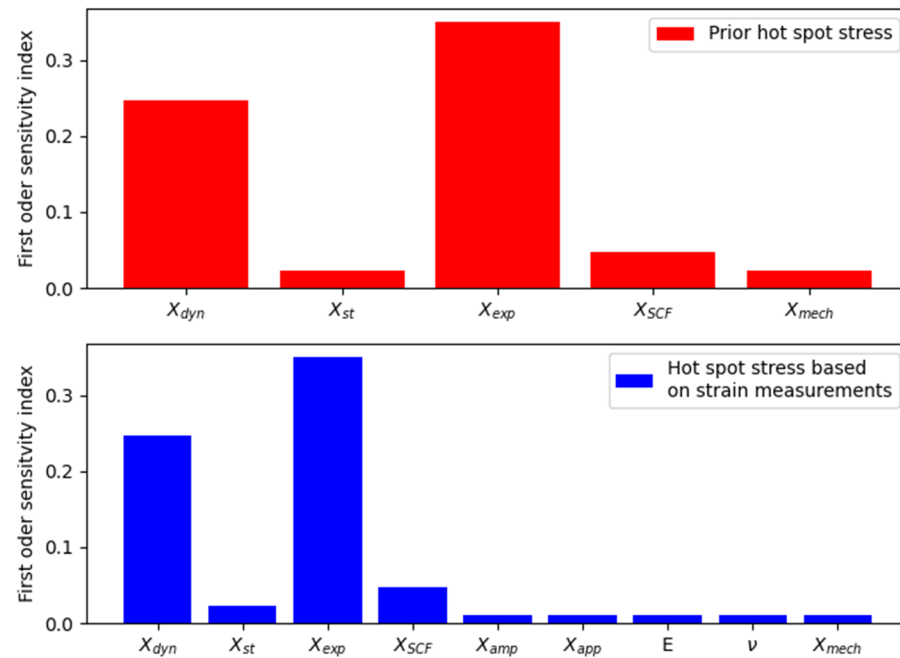


Figure 11. Sensitivity indexes for the random variables influencing the hot spot stress (prior and based on strain measurements).

The uncertainty, X_{exp} , in the modelling of the exposure has the highest influence on the nominal stress (prior and based on strain measurements), followed by the uncertainty, X_{dyn} , related to modelling of the dynamics. The uncertainties in the strain measurement, summarized as X_{app} and X_{amp} , and the uncertainty in the material model, given by E and ν , have a very small influence on the hot spot stress similar to the uncertainty in the mechanical model, X_{mech} .

Due to the small influence of the strain measurement and material uncertainties, the probability density function of the stress ranges based on strain measurements does not differ very much from the prior PDF of the stress ranges.

5.2. Prior and Predicted Posterior Fatigue Reliability of a Welded Joint

Based on the prior and predicted posterior stress range distributions, $f(\Delta\sigma_{Design})$ and $f(\Delta\sigma_{Design}|\Delta\sigma_M)$, the reliability of the welded joint can be determined.

The limit state equation considering each wind direction and the probability of occurrence is given as:

$$g(\mathbf{X}_{SN}, t) = \Delta - \nu \cdot t \sum_{j=1} p_j \cdot E_j[\Delta D_i] \quad (51)$$

where p_j is the probability of occurrence of the wind direction and $E_j[\Delta D_i]$ is the corresponding damage increment (Equation (37)). The uncertainty in the underlying SN curve is given by fatigue design of the steel structures standard by DNVGL [30]. The characteristic bi-linear SN curve for the structures is described by negative inverse slopes $m_1 = 3$ and $m_2 = 5$ and the intercepts $\log K_{C1} = 12.18$ and $\log K_{C2} = 16.13$. The mean SN curve for probabilistic calculation is determined from the characteristic SN curve, assuming a standard deviation of $s_{\log N} = 0.2$.

$$\log K_i = \log K_{Ci} + 2 \cdot s_{\log N} \quad (52)$$

Both SN curves are shown in Figure 12.

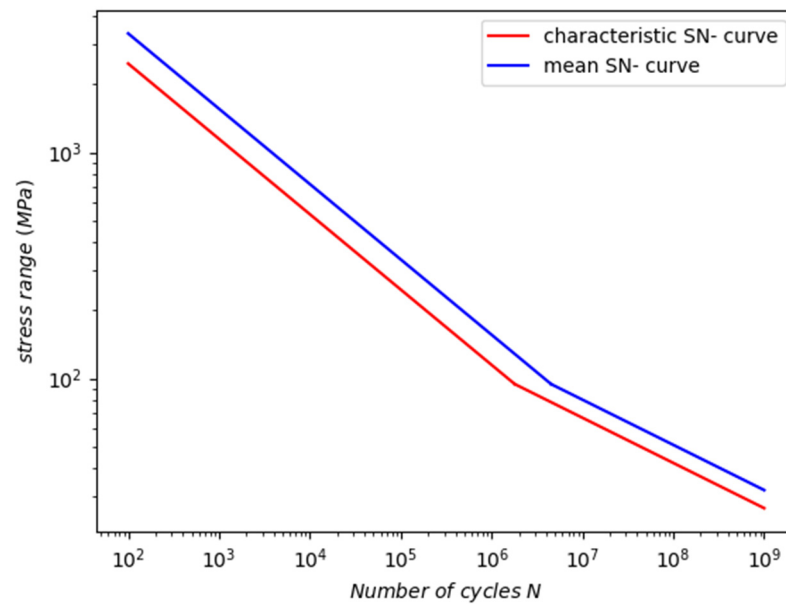


Figure 12. Bi-linear characteristic and mean SN curves for structures located in seawater environments with cathodic protections.

Based on the limit state function (Equation (51)), a failure occurs if $g(\mathbf{X}_{SN}, t) \leq 0$ with $\mathbf{X}_{SN} = [\Delta, K_1, K_2, B_Q]^T$. The probabilistic model parameters, together with the deterministic parameters applied for the reliability calculation of the numerical study, are summarized in Table 4.

Table 4. Probabilistic and deterministic parameters for the calculation for the reliability index and the cumulative probability of failure.

Parameter		Unit	Distribution	Values	Reference
Number of stress cycles	ν	-	deterministic	1.5×10^7	
Inverse slopes of the SN curve	m_1	-	deterministic	3	[30]
	m_2	-	deterministic	5	[30]
SN curve intercepts	$\log K_1$	-	normal	$\mu = 12.45$	$\sigma = 0.2$ [30]
	$\log K_2$	-	normal	$\mu = 16.48$	$\sigma = 0.2$ [30]
Detail quality	B_Q	-	lognormal	$\mu = 1$	$\sigma = 0.37$ [41]
SN fatigue limit	Δ	-	lognormal	$\mu = 1$	$\sigma = 0.3$ [30]

For the given prior stress range distribution, $f(\Delta\sigma_{Design})$, and the determined predicted posterior stress range distribution, $f(\Delta\sigma_{Design} | \Delta\sigma_M)$, the event of failure is calculated in a Monte Carlo Simulation (MCS) with 10^8 simulations, varying the uncertain parameters of the damage increment and the limit state function. Over a service life of 25 years, the following cumulative probabilities of failure and reliability are determined for position 1 (Figure 13).

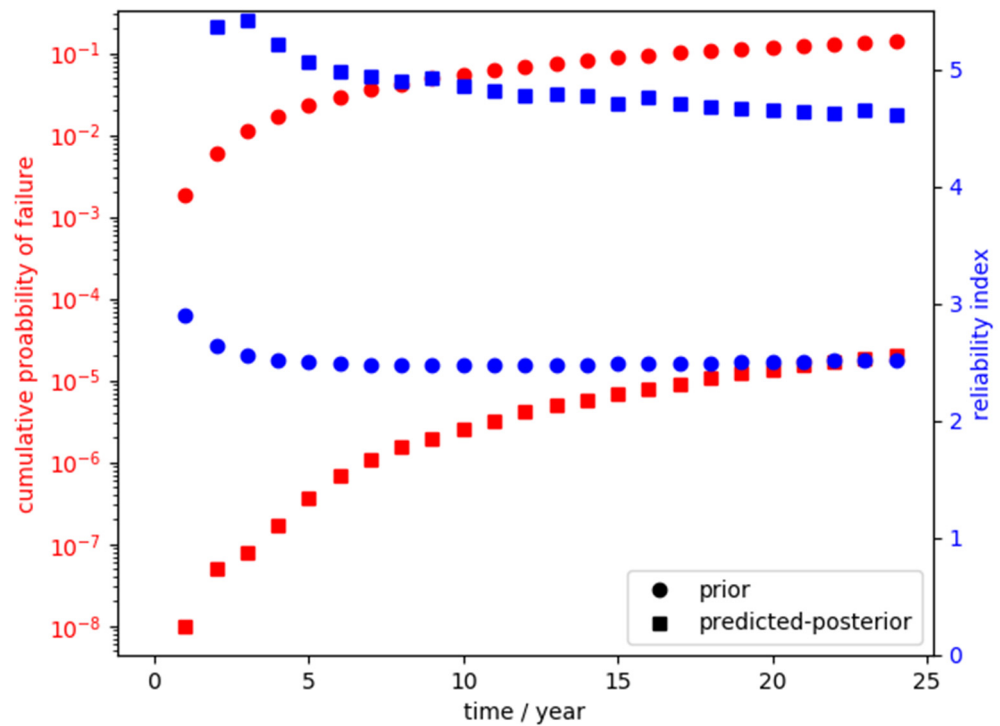


Figure 13. Cumulative probability of failure and annual reliability index of the welded joint determined for the prior stress range distribution, $f(\Delta\sigma_{Design})$, and the predicted posterior stress range distribution, $f(\Delta\sigma_{Design}|\Delta\sigma_M)$, over the service life at position 1.

According to Figure 13, the cumulative probability of failure of the prior stress ranges has larger values than the cumulative probability of failure of the predicted posterior stress ranges (red curves). On the other hand, the reliability indexes of the predicted posterior stress ranges achieve higher values in comparison to the indexes of the prior stress ranges (blue curves).

To determine the influence of the uncertainty parameters on the limit state function, a sensitivity analysis determining the first order sensitivity index was performed [53]. The influence of the input parameters over the service life is shown in Figure 14.

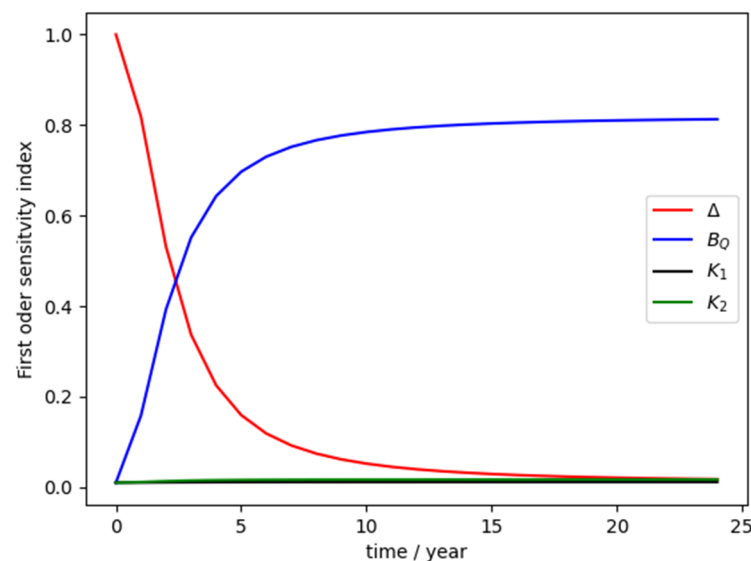


Figure 14. Sensitivity indexes for the uncertain parameters influencing the limit state equation.

At the beginning of the service life, the SN fatigue limit, Δ , shows the highest influence, but then decreases approximately exponentially. The uncertainty in quality of detail, B_Q , is at the beginning is very low, but then increases, before it is approximately constant at the end. The SN curve intercepts K_1 and K_2 have only a minor influence on the limit state function over the service life.

6. Summary and Concluding Remarks

This article contains a fatigue reliability analysis of a welded joint based on predicted posterior stress ranges, which are determined from predicted strain measurements of turbine support structures. From the calculation of the predicted posterior probabilities, the developed approach facilitates the integration in a pre-posterior decision analysis.

In the first part, an approach for the determination of the continuous predicted posterior stress range distribution of a welded connection of a wind turbine with a fixed support structure is presented. Based on the information of the stress resultants from the design, the continuous prior stress range distribution is determined considering uncertainties in the overall dynamic simulation, the mechanical model and the stress concentration factor. The prior distribution is updated with stress ranges based on predicted measured strains, which are derived from the data on the stress resultants from the design. Using the material and mechanical models, considering uncertainties in the strain measurement and the material and mechanical models, as well as the stress concentration factor, the continuous predicted posterior stress range distribution is determined by applying Bayesian updating. The difference between the prior stress range distribution and the stress ranges based on strain measurements is very small, as the influence of the overall dynamic simulation uncertainties is dominant and the influence of other uncertainties is small. The order of uncertainties is similar for prior stress ranges and the predicted stress ranges based on strain measurements. A reduction in uncertainty of predicted strain measurements does not take place, as the stress ranges are based on the dominant stress resultants from the design. After posterior updating, the prior stress range distribution, the probability of smaller stress ranges increases, while the occurrence of higher stress ranges decreases. Furthermore, the presented approach is also applicable or the investigation of welded joints of other support structures, such as jacket structures or floating structures, if the stress resultants from the design are available.

In the second part, the prior and the predicted posterior stress ranges are utilized in a fatigue reliability calculation. The event of failure for the SN approach is defined based on a limit state function. Considering uncertainty in the quality of detail, in the fatigue limit and the underlying SN curve itself, the cumulative probability of failure for the prior and predicted posterior stress ranges over the service life is determined. Based on the annual probability of failure, the reliability index is calculated. The posterior fatigue reliability is higher than the prior fatigue reliability from the design. In comparison with the scientific literature, similar reliability increases depending on the uncertainty of additional information are found [3,54].

The approach presented in Section 3 allows the prediction of strain measurements in support structures of wind turbines using stress resultant design data. The predicted strains can be used to update the prior stress ranges to the predicted posterior stress ranges. This enables the calculation of the posterior reliability to make predictions about the future structural reliability before the measurement system is installed. Moreover, the predicted strain measurements or updated stress ranges can be used as input in a pre-posterior decision analysis to forecast the optimal inspection strategy (e.g., to determine the inspection time of welded joint) or to make statements about the future positioning of strain gauges of the monitoring system.

Author Contributions: M.K.: original draft and writing; S.T.: supervision. All authors have read and agreed to the published version of the manuscript.

Funding: This work was supported by the Federal Ministry for Economic Affairs and Climate Action through grant 03SX449Z.

Data Availability Statement: The used data can be found in the cited references.

Conflicts of Interest: The authors declare no conflict of interest.

Appendix A

Table A1. Characteristic parameters of the prior stress ranges, $f(\Delta\sigma_{Design})$, depending on the wind direction.

Wind Direction		Position 1		Position 2		Position 3		Position 4	
		Shape	Scale, N/m ²	Shape	Scale, N/m ²	Shape	Scale, N/m ²	Shape	Scale, N/m ²
North	(N)	1.03	5.11×10^{-2}	0.67	3.04×10^6	0.67	4.30×10^6	0.67	3.04×10^6
North east	(NE)	0.71	3.84×10^6	0.71	5.43×10^6	0.71	3.84×10^6	1.04	5.12×10^{-2}
East	(E)	0.75	5.27×10^6	0.75	3.73×10^6	1.04	5.17×10^{-2}	0.75	3.73×10^6
East south	(ES)	0.73	3.17×10^6	1.04	5.12×10^{-2}	0.73	3.17×10^6	0.73	4.48×10^6
South	(S)	1.04	5.16×10^{-2}	0.73	3.48×10^6	0.73	4.92×10^6	0.73	3.48×10^6
South west	(SW)	0.74	4.50×10^6	0.74	6.36×10^6	0.74	4.50×10^6	1.04	5.12×10^{-2}
West	(W)	0.73	6.65×10^6	0.73	4.70×10^6	1.04	5.14×10^{-2}	0.73	4.70×10^6
West north	(WN)	0.69	3.43×10^6	1.04	5.12×10^{-2}	0.69	3.43×10^6	0.69	4.85×10^6

Wind Direction		Position 5		Position 6		Position 7		Position 8	
		Shape	Scale, N/m ²	Shape	Scale, N/m ²	Shape	Scale, N/m ²	Shape	Scale, N/m ²
North	(N)	1.03	5.11×10^{-2}	0.67	3.04×10^6	0.67	4.30×10^6	0.67	3.04×10^6
North east	(NE)	0.71	3.84×10^6	0.71	5.43×10^6	0.71	3.84×10^6	1.04	5.12×10^{-2}
East	(E)	0.75	5.27×10^6	0.75	3.73×10^6	1.04	5.17×10^{-2}	0.75	3.73×10^6
East south	(ES)	0.73	3.17×10^6	1.04	5.12×10^{-2}	0.73	3.17×10^6	0.73	4.48×10^6
South	(S)	1.04	5.16×10^{-2}	0.73	3.48×10^6	0.73	4.92×10^6	0.73	3.48×10^6
South west	(SW)	0.74	4.50×10^6	0.74	6.36×10^6	0.74	4.50×10^6	1.04	5.12×10^{-2}
West	(W)	0.73	6.65×10^6	0.73	4.70×10^6	1.04	5.14×10^{-2}	0.73	4.70×10^6
West north	(WN)	0.69	3.43×10^6	1.04	5.12×10^{-2}	0.69	3.43×10^6	0.69	4.85×10^6

References

- Hau, E. *Wind Turbines: Fundamentals, Technologies, Application, Economics*; Springer Science & Business Media: Berlin/Heidelberg, Germany, 2013.
- Burton, T.; Jenkins, N.; Sharpe, D.; Bossanyi, E. *Wind Energy Handbook*; John Wiley & Sons: Hoboken, NJ, USA, 2011.
- Farhan, M.; Schneider, R.; Thöns, S. Predictive information and maintenance optimization based on decision theory: A case study considering a welded joint in an offshore wind turbine support structure. *Struct. Health Monit.* **2021**, *21*, 185–207. [\[CrossRef\]](#)
- Bismut, E.; Straub, D. Optimal adaptive inspection and maintenance planning for deteriorating structural systems. *Reliab. Eng. Syst. Saf.* **2021**, *215*, 107891. [\[CrossRef\]](#)
- Straub, D. Value of information analysis with structural reliability methods. *Struct. Saf.* **2014**, *49*, 75–85. [\[CrossRef\]](#)
- Schlaifer, R.; Raiffa, H. *Applied Statistical Decision Theory*; Harvard University Press: Boston, MA, USA, 1961.
- Eichner, L.; Schneider, R.; Simon, P.; Baeßler, M. Optimal sensor placement for vibration-based structural health monitoring obtained via value of information analysis as part of a digital structural integrity management of offshore structures. In Proceedings of the 3rd International Conference on Health Monitoring of Civil & Maritime Structures (HeaMES 2022), Edinburgh, UK, 8–9 June 2022; pp. 23–32.
- Pozzi, M.; Der Kiureghian, A. Assessing the value of information for long-term structural health monitoring. In *Health Monitoring of Structural and Biological Systems*; International Society for Optics and Photonics; SPIE: Bellingham, WA, USA, 2011.
- Faber, M.H.; Thöns, S. On the Value of Structural Health Monitoring. In Proceedings of the 22nd Annual Conference on European Safety and Reliability, Amsterdam, The Netherlands, 29 September–2 October 2013.
- Sousa, H.; Wenzel, H.; Thöns, S. Quantifying the Value of Structural Health Information for Decision Support: TU1402 Guide for Operators. COST Action TU1402. 2019. Available online: www.cost-tu1402.eu/action/deliverables/guidelines (accessed on 3 May 2021).
- Zhang, W.-H.; Lu, D.-G.; Qin, J.; Thöns, S.; Faber, M.H. Value of information analysis in civil and infrastructure engineering: A review. *J. Infrastruct. Preserv. Resil.* **2021**, *2*, 16. [\[CrossRef\]](#)
- Hong, H.P. Reliability Analysis with Nondestructive Inspection. *Struct. Saf.* **1997**, *19*, 383–395. [\[CrossRef\]](#)

13. Beck James, L.; Au, S.-K. Bayesian Updating of Structural Models and Reliability using Markov Chain Monte Carlo Simulation. *J. Eng. Mech.* **2002**, *128*, 380–391. [[CrossRef](#)]
14. Ching, J.; Chen, Y.-C. Transitional Markov Chain Monte Carlo Method for Bayesian Model Updating, Model Class Selection, and Model Averaging. *J. Eng. Mech.* **2007**, *133*, 816–832. [[CrossRef](#)]
15. Straub, D.; Papaioannou, I. Bayesian updating with structural reliability methods. *J. Eng. Mech.* **2015**, *141*, 04014134. [[CrossRef](#)]
16. Küttenbaum, S.; Braml, T.; Taffe, A.; Keßler, S.; Maack, S. Reliability assessment of existing structures using results of nondestructive testing. *Struct. Concr.* **2021**, *22*, 2895–2915. [[CrossRef](#)]
17. Thöns, S.; Irman, A.A.; Limongelli, M.P. On Uncertainty, Decision Values and Innovation. In Proceedings of the International Conference on Uncertainty in Mechanical Engineering (ICUME), Darmstadt, Germany, 7–8 June 2021; pp. 252–263.
18. Clormann, U.; Seeger, T. Rainflow-HCM. Ein Zählverfahren für Betriebsfestigkeitsnachweise auf werkstoffmechanischer Grundlage. *STAHLBAU DER* **1986**, *55*, 65–71.
19. GmbH, H.B.M. Optische Dehnungssensoren—Grundlagen. Available online: https://www.hbm.com/de/7256/optische-dehnungssensoren-grundlagen/?utm_term=&utm_campaign=Leads_Performance_Max_Torque_T210_DE&utm_source=adwords&utm_medium=ppc&hsa_acc=3043843200&hsa_cam=18824231000&hsa_grp=&hsa_ad=&hsa_src=x&hsa_tgt=&hsa_kw=&hsa_mt=&hsa_net=adwords&hsa_ver=3&gclid=EAIaIQobChMI9piH2rXx_AIVSPBRCh2IWA5wEAAYAiAAEgJk3PD_BwE (accessed on 10 January 2023).
20. Mühl, T. *Einführung in Die Elektrische Messtechnik: Grundlagen, Messverfahren, Anwendungen*; Springer: Berlin/Heidelberg, Germany, 2014.
21. Choi, H.; Choi, S.; Cha, H. Structural health monitoring system based on strain gauge enabled wireless sensor nodes. In Proceedings of the 2008 5th International Conference on Networked Sensing Systems, Ikanazawa, Japan, 17–19 June 2008; pp. 211–214.
22. Enright, M.P.; Hudak, S.J.; McClung, R.C.; Millwater, H.R. Application of probabilistic fracture mechanics to prognosis of aircraft engine components. *AIAA J.* **2006**, *44*, 311–316. [[CrossRef](#)]
23. Thöns, S.; Faber, M.; Rucker, W. On the utilization of monitoring data in an ultimate limit state reliability analysis. In Proceedings of the 11th International Conference on Applications of Statistics and Probability in Civil Engineering (ICASP)(Zurich), Dublin, Ireland, 9–13 July 2023.
24. Söker, H. Ermittlung von Ermüdungslasten an großen Windenergieanlagen. *DEWI Mag* **1996**, *8*, 44–48.
25. Pollino, M.C.; Huckelbridge, A.A. In-situ measurements of fatigue demands on a wind turbine support structure. In Proceedings of the 2012 IEEE Energytech, Cleveland, OH, USA, 29–31 May 2012; pp. 1–5.
26. Tarp-Johansen, N.; Madsen, P.H.; Frandsen, S.T. Calibration of partial safety factors for extreme loads on wind turbines. In Proceedings of the 2003 European Wind Energy Conference and Exhibition, Madrid, Spain, 16–19 June 2003.
27. Velarde, J.; Kramhöft, C.; Sørensen, J.D.; Zorzi, G. Fatigue reliability of large monopiles for offshore wind turbines. *Int. J. Fatigue* **2020**, *134*, 105487. [[CrossRef](#)]
28. JCSS Joint Committee on Structural Safety. Probabilistic Model Code. 2001–2015. Available online: <https://www.jcss-lc.org/jcss-probabilistic-model-code/> (accessed on 2 February 2022).
29. Veritas, B. Rules for the Classification of Steel Ships; The Bureau. 2000. Available online: https://erules.veristar.com/dy/data/bv/pdf/467-NR_PartB_2022-07.pdf (accessed on 13 January 2022).
30. DNV GL Group. *DNVGL-RP-C203—Fatigue Design of Offshore Steel Structures*; DNV GL Group: Bærum, Norway, 2016.
31. Kinne, M.; Schneider, R.; Thöns, S. *Reconstructing Stress Resultants in Wind Turbine Towers Based on Strain Measurements*; Springer International Publishing: Cham, Switzerland, 2021; pp. 224–235.
32. Keil, S. *Beanspruchungsermittlung Mit Dehnungsmessstreifen*; Cuneus: Zwingenberg, Germany, 1995.
33. Thöns, S. Monitoring based condition assessment of offshore wind turbine support structures. *IBK Bericht Nr.* **2012**, *345*, 99–117.
34. Tokyo Measuring Instruments Laboratory Co. Ltd. *TML WFLA-6-17 Strain Gauge Test Data*; Tokyo Measuring Instruments Laboratory Co. Ltd.: Tokyo, Japan, 2008.
35. HBM GmbH. MGCplus—Measuring amplifier system. In *Special Features*; HBM GmbH: Darmstadt, Germany, 2020.
36. Naess, A.; Moan, T. *Stochastic Dynamics of Marine Structures*; Cambridge University Press: Cambridge, UK, 2013.
37. Madsen, H.; Krenk, S.; Lind, N. *Methods of Structural Safety*; Dover New York: New York, NY, USA, 1986.
38. Khan, R.A.; Ahmad, S. Bi-linear fatigue and fracture approach for safety analysis of an offshore structure. *J. Offshore Mech. Arct. Eng.* **2014**, *136*. [[CrossRef](#)]
39. Schneider, R.; Rogge, A.; Thöns, S. *SysPark—System Model for Offshore Wind Park Support Structures*; Bundesanstalt für Materialforschung und -prüfung (BAM): Berlin, Germany, 2019.
40. Straub, D. *Generic Approaches to Risk Based Inspection Planning for Steel Structures*; vdf Hochschulverlag AG: Munich, Germany, 2004; Volume 284.
41. Folsø, R.; Otto, S.; Parmentier, G. Reliability-based calibration of fatigue design guidelines for ship structures. *Mar. Struct.* **2002**, *15*, 627–651. [[CrossRef](#)]
42. Sørensen, J.; Toft, H. *Safety Factors—IEC 61400—1 ed. 4—Background document*; Technical University of Denmark (DTU): Lyngby, Denmark, 2014.
43. International, M.O. *Baltic Sea-In Situ Near Real Time Observations*; International, M.O., Ed.; Mercator Ocean International: Ramonville Saint-Agne, France, 2015. [[CrossRef](#)]

44. Describing Wind Variations: Weibull Distribution. Available online: <http://www.xn--drmstrre-64ad.dk/wp-content/wind/miller/windpower%20web/en/tour/wres/weibull.htm> (accessed on 24 February 2022).
45. Soto-Rivas, K.; Richter, D.; Escauriaza, C. A formulation of the thrust coefficient for representing finite-sized farms of tidal energy converters. *Energies* **2019**, *12*, 3861. [[CrossRef](#)]
46. IEC 61400-1:2005; Wind turbines. Part 1: Design Requirements. European Committee for Electrotechnical Standardization: Brussels, Belgium, 2005.
47. Wölfel Engineering GmbH + Co. KG. Fatigue Parameters of Arkona Becken OWF wind turbines for the MISO project. In *Internal MISO Project Report*; Wölfel Engineering GmbH + Co. KG: Höchberg, Germany, 2020.
48. Geotechnik, I.f. IGtHPile. Available online: <https://www.igth.uni-hannover.de/download.html> (accessed on 23 October 2019).
49. Reese, L.; Cox, W.; Koop, F. Field Testing of Laterally Loaded Piles in Stiff Clay. In *Proceedings of the 7th Annual Offshore Technology Conference*, Houston, TX, USA, 5–7 November 2018; pp. 671–690.
50. Altamura, A.; Straub, D. Reliability assessment of high cycle fatigue under variable amplitude loading: Review and solutions. *Eng. Fract. Mech.* **2014**, *121*, 40–66. [[CrossRef](#)]
51. Verein Deutscher Ingenieure/Verband der Elektrotechnik Elektronik Informationstechnik. VDI/VDE 2635 Part 1. In *Experimental Structure Analysis-Metallic Bonded Resistance Strain Gages—Characteristics and Testing Conditions*; Verein Deutscher Ingenieure: Harzgerode, Germany, 2007.
52. Spodarev, E. Stochastik I—Vorlesungsskript. University of Ulm. 2016. Available online: https://www.uni-ulm.de/fileadmin/website_uni_ulm/mawi.inst.110/mitarbeiter/spodarev/publications/scripts/Stochastik1_16.12.2016.pdf (accessed on 7 September 2022).
53. Sobol', I.y.M. On sensitivity estimation for nonlinear mathematical models. *Mat. Model.* **1990**, *2*, 112–118.
54. Schneider, R. *Time-Variant Reliability of Deteriorating Structural Systems Conditional on Inspection and Monitoring Data*; Technische Universität München: München, Germany, 2019.

Disclaimer/Publisher's Note: The statements, opinions and data contained in all publications are solely those of the individual author(s) and contributor(s) and not of MDPI and/or the editor(s). MDPI and/or the editor(s) disclaim responsibility for any injury to people or property resulting from any ideas, methods, instructions or products referred to in the content.